Acta Biomaterialia 68 (2018) 99–112

Contents lists available at ScienceDirect

Acta Biomaterialia

journal homepage: www.elsevier.com/locate/actabiomat

Full length article

Nanoparticle-induced inflammation can increase tumor malignancy

Bella B. Manshian [a], Jennifer Poelmans [a], Shweta Saini [a], Suman Pokhrel [b], Julio Jiménez Grez [c,d], Uwe Himmelreich [a], Lutz Mädler [b], Stefaan J. Soenen [a,*]

[a] Biomedical MRI Unit/MoSAIC, Department of Imaging and Pathology, KU Leuven, Herestraat 49, B3000 Leuven, Belgium
[b] Foundation Institute of Materials Science (IWT), Department of Production Engineering, University of Bremen, Bremen, Germany
[c] Organ Systems, Department of Development and Regeneration, KU Leuven, Herestraat 49, B3000 Leuven, Belgium
[d] Department of Obstetrics and Gynaecology, Clínica Alemana Universidad del Desarrollo, Santiago, Chile

ARTICLE INFO

Article history:
Received 30 August 2017
Received in revised form 12 December 2017
Accepted 15 December 2017
Available online 20 December 2017

Keywords:
Nanoparticle shape
Inflammation
Tumor metastasis
Aluminum oxide nanoparticles

ABSTRACT

Nanomaterials, such as aluminum oxide, have been regarded with high biomedical promise as potential immune adjuvants in favor of their bulk counterparts. For pathophysiological conditions where elevated immune activity already occurs, the contribution of nanoparticle-activated immune reactions remains unclear. Here, we investigated the effect of spherical and wire-shaped aluminum oxide nanoparticles on primary splenocytes and observed a clear pro-inflammatory effect of both nanoparticles, mainly for the high aspect ratio nanowires. The nanoparticles resulted in a clear activation of NLRP3 inflammasome, and also secreted transforming growth factor β. When cancer cells were exposed to these cytokines, this resulted in an increased level of epithelial-to-mesenchymal-transition, a hallmark for cancer metastasis, which did not occur when the cancer cells were directly exposed to the nanoparticles themselves. Using a syngeneic tumor model, the level of inflammation and degree of lung metastasis were significantly increased when the animals were exposed to the nanoparticles, particularly for the nanowires. This effect could be abrogated by treating the animals with inflammatory inhibitors. Collectively, these data indicate that the interaction of nanoparticles with immune cells can have secondary effects that may aggravate pathophysiological conditions, such as cancer malignancy, and conditions must be carefully selected to finely tune the induced aspecific inflammation into cancer-specific antitumor immunity.

Statement of Significance

Many different types of nanoparticles have been shown to possess immunomodulatory properties, depending on their physicochemical parameters. This can potentially be harnessed as a possible antitumor therapy. However, in the current work we show that inflammation elicited by nanomaterials can have grave effects in pathophysiological conditions, where non-specific inflammation was found to increase cancer cell mobility and tumor malignancy. These data show that immunomodulatory properties of nanomaterials must be carefully controlled to avoid any undesired side-effects.

1. Introduction

Nanoparticle (NP) aspect ratio plays an important role in the biological activity of nanosized materials [1–3]. In particular, the biodistribution, toxicity and immune reactions of NPs have been shown to be distinctively linked to their aspect ratio [4,5]. High aspect ratio NPs such as carbon nanotubes, have been found to activate the NLRP3 inflammasome, which can trigger pulmonary toxicity by fibrosis [6]. Various other inorganic high aspect ratio NPs have been described to display aspect ratio-dependent toxicity, both *in vitro* and *in vivo*, including cerium oxide (CeO_2) nanorods [6], silicon [7], nickel [8] or silver nanowires [9] and alumina nanotubes [10]. Some results cannot solely be ascribed to differences in aspect ratios as some NPs also differed in other factors such as surface activity [11–13]. A recent systematic study on nanosized anodic alumina nanotubes revealed that long nanotubes triggered enhanced cell death and inflammation than shorter nanotubes [10].

Anodic alumina nanostructures are generally considered as a non-hazardous biomaterial due to its highly inert chemical composition, resulting in its commercial use for biomedical applications

* Corresponding author.
E-mail address: s.soenen@kuleuven.be (S.J. Soenen).

https://doi.org/10.1016/j.actbio.2017.12.020
1742-7061/

[14]. Aluminum oxide (AlO) NPs are listed among 14 high-priority nanomaterials published by the Organization for Economic Co-operation and Development to be studied regarding their potential toxicity [4]. The biomedical use of AlO NPs is increasing rapidly, where bulk alum (aluminum hydroxide, phosphate, or hydroxyphosphate) has been used as an adjuvant for more than 60 years and is currently the most widely used adjuvant in both veterinary and human vaccines [15]. Bulk alum therefore has a longstanding and excellent safety record for systemic administration, which has also stimulated the use of nanosized AlO NPs. The latter have been shown to increase specific anti-cancer immune responses in comparison to bulk alum [15]. AlO NPs may therefore soon replace the adjuvants in antiviral vaccines [16]. Nanometric AlO coatings on ferromagnetic cores were also found to improve their biocompatibility, enabling efficient thermal therapy [17]. Another key application of AlO NPs lies in their use in dental or medical implants. AlO NPs have been found to increase the mechanical resistance to wear and the increased surface area promotes osseointegration and reduces graft rejection [18,19]. AlO NP can also be released from porous aluminum sheets, which are increasingly investigated for tissue engineering [20] and drug delivery purposes [21].

The increasing interest in AlO NPs for biomedical use stems from their low level of cytotoxicity, where AlO NPs have been described to be biologically inert [22]. This in itself is of course slightly contradictory to the intrinsic potent activation of the inflammasome by AlO NPs. Activation of the NLRP3 inflammasome can have widely varying consequences, as it has been shown to be a transcriptional regulator of Th2 differentiation [23] and it is released as a particulate danger signal that amplifies inflammatory responses [12,24], thereby potentially aggravating any intrinsic inflammation that already pre-existed in the body.

One key question that remains is whether the use of potent immune-modulating NPs, and in particular high aspect ratio ones, may have any implications on inflammatory conditions. The onset of cancer is typically associated with high levels of inflammation [25]. As a major application for nanosized AlO is to act as an immune adjuvant for cancer therapy, the intrinsic effects of the AlO NPs on the tumor itself remains an open question. Here, we investigate for the first time the effect of AlO NPs (spheres (NS) and wires (NW))-mediated inflammation on tumor cells, and observed clear effects of the AlO NWs on tumor cell metastasis, both *in vitro* and *in vivo*, which correlated with the level of induced inflammation.

2. Materials and methods

2.1. Nanoparticles and nanoparticle characterization

AlO NSs and NWs were purchased from Sigma Aldrich (Diegem, Belgium). The NWs were provided as dry powder with 2–6 nm diameter and 200–400 nm length. The NSs (diameter: 30–60 nm) were provided as a 20% suspension in pure H_2O.

For the TEM specimen preparation, a drop of nanoparticle solution was dropped on the Cu-grid with C-film for the TEM investigation. For the powder samples, small portion of the powder (~1–2 mg) was dispersed in 5 mL of ethanol (Strem Chemicals, AR grade) in an ultrasonic bath and sonicated for 15 min. A drop of the dispersed sample was dropped on the Cu grid. All the grids with the sample were dried at RT followed by scanning the large regions of the grid. The low and high resolution TEM of the sample were examined using transmission electron microscopy (TEM) on a FEI Titan 80/300 microscope equipped with a Cs corrector for the objective lens, a Fischione high angle annular dark field detector (HAADF), GATAN post-column imaging filter and a cold field emission gun operated at 300 kV as an acceleration voltage. On selected samples, energy-dispersive X-ray spectroscopy (EDS) was performed to determine the chemical composition of the visualized specimens.

For inductively coupled plasma-mass spectrometry (ICP-MS) analysis, samples were exposed to 0.5 mL of aqua regia. The samples were then microwave digested (MLS 1200 Mega, Milestone, Shelton, CT, USA) and appropriately diluted in ultrapure water (> 18.2 MΩ cm resistivity). Iridium (Merck, Darmstadt, Germany) was added as an internal standard (final concentration: 2 μg/L). External calibration was applied to quantify the amount of elemental aluminum. An external standard was obtained by diluting a standard aluminum solution (ALFA Johnson Matthey, Karlsruhe, Germany) in the same background solution as the samples. All samples were measured in triplicate using the following settings: rf power: 1,150 W, plasma gas flow rate: 15 L/min, auxiliary gas flow rate: 0.85 L/min, nebulizer gas flow rate: 1.15 L/min. For sample introduction, a MicroMist nebulizer (200 μL/min) and a cyclonic spray chamber both from Glass Expansion (Pocasset, MA, USA) were used.

2.2. Preparation of NP suspension

AlO NP stock solutions were first prepared in DI H_2O at 5 mg/mL. For cell exposure studies, all NP suspensions were freshly prepared by 10 min probe sonication of the stock solutions followed by adding the required aliquot of the stock solution to the full culture medium of the cells.

2.3. Cell culture

In the present study, the following cancer cell types were used: murine lung squamous tumor cells (KLN 205), human cervical cancer cells (HeLa), human alveolar adenocarcinoma cells (A549) and human epithelial ovarian cancer cells (SKOV3). HeLa and A549 cells were cultured in high glucose containing Dulbecco's modified Eagle's medium (DMEM), supplemented with 10% fetal calf serum, 1 mM sodium pyruvate, 2 mM L-glutamine, and 1% penicillin/streptomycin (Gibco, Invitrogen, Belgium). KLN 205 and SKOV3 cells were cultured in high glucose DMEM, supplemented with 10% fetal calf serum, 1 mM sodium pyruvate, 2 mM L-glutamine, 1% non-essential amino acids and 1% penicillin/streptomycin. All cell types were maintained in a humidified atmosphere at 37 °C and 5% CO_2 and split 1/5 upon reaching 80% confluency.

Whole splenocyte suspension was prepared by grinding up spleens isolated from C57/Bl6 mice of 7 weeks old with frosted glasses and cell strainers (BD Biosciences). Red blood cells were lysed after centrifugation at 1,200 rpm for 5 min. Then, splenocytes were counted using a hemocytometer and maintained in RPMI 1640 medium supplemented with 10% FBS.

2.4. Cellular composition of splenocytes by flow cytometry

Isolated splenocytes were transferred to 10% serum-containing PBS, after which the cells were exposed to anti-CD16/32 antibody to block the Fc receptors on the cells. To determine the different subpopulations in the splenocytes, the cells were subsequently exposed to a mixture of FITC-conjugated anti-CD3 (T cell marker), PerCPCy5.5-conjugated anti-F480 (macrophage marker), AF-780 conjugated anti-CD45 (leukocyte marker), AF-450 conjugated anti-CD11b (pan macrophage marker). 30 mins post antibody exposure, cells were isolated by repeated centrifugation and washing steps, after which the cells were analyzed using flow cytometry (Gallios flow cytometer, Beckman Coulter, Suarlée, Belgium).

2.5. Cell-nanoparticle interaction studies by high-content analysis

The cancer cell types were seeded at 3000 cells/well in a 96 well plate (Nunc, Belgium) after which the cells were allowed to attach overnight in a humidified atmosphere at 37 °C and 5% CO_2. Then, the cells were incubated with the different AlO NPs for 24 h in their full growth medium at a concentration of 0–200 μg/mL for AlO NSs and 0–450 μg/mL for AlO NWs. The immune cells were seeded at 100,000 cells/well in a 24 well plate (Nunc, Belgium) after which the cells were primed with 10 ng/mL lipopolysaccharide (LPS; InVivoGen) for 12 h followed by exposure to the AlO NPs in their full growth medium at a concentration of 0–200 μg/mL for AlO NSs and 0–450 μg/mL for AlO NWs for 8 h to reduce the degree of cell death associated to prolonged culture of primary splenocytes. For dexamethasone (Sigma-Aldrich, Bornem, Belgium), LPS-primed splenocytes were exposed to the AlO NPs similarly as described above, where the medium was further supplemented with 100 ng/mL dexamethasone. Galunisertib experiments were carried out identically to dexamethasone treatments, where galunisertib (LY2157299, Selleck Chemicals, USA) was provided at 25 ng/ml. Every condition was performed in triplicate and results were analyzed based on 4 independent repeats. The high-content imaging experiments were then performed based on previously validated methods as described elsewhere [26–28].

2.6. Caspase-1 activation

Active caspase-1 was detected fluorometrically using the caspase-1 flurochrome inhibitor of caspases (FLICA) kit from Immunochemistry Technologies. Briefly, LPS-primed splenocytes ($1*10^6$/mL) were treated with either PBS, AlO NSs (125 μg/mL) or AlO NWs (300 μg/mL) for 8 h after which the cells were treated with the fluorescein-labeled inhibitor FAM-YVAD-fmk (5-carboxy fluorescein-Tyr-Val-Ala-Asp-fluoromethyl ketone) for 1 h at 37 °C. The cells were then washed three times with PBS and fluorescence levels were measured by a fluometric plate reader using fluorescein filters (Optima FluoStar, BMG LabTech GmbH, Ortenberg, Germany).

2.7. Evaluation of IL1β and IL18 cytokine secretion by splenocytes

Splenocytes were plated in 6 well plates at 500,000 cells/well, after which they were primed with LPS (10 ng/ml) for 12 h prior to being exposed to either PBS, AlO NSs (125 μg/mL) or AlO NWs (300 μg/mL) for 8 h. Culture supernatants were then collected, centrifuged for 5 min at 5,000 rpm to remove cells, and assessed for IL-1β and IL18 protein content by ELISA following the manufacturer's protocol (IL1β: R&D Systems, Minneapolis, MN, USA; IL18: MBL International, Woburg, MA, USA). Absorbance was recorded at 450 and 570 nm with an ELISA plate reader (Optima FluoStar, BMG LabTech GmbH, Ortenberg, Germany).

2.8. Induction of EMT in cancer cells

Splenocytes were plated in 24 well plates at 100,000 cells/well, after which they were primed with LPS (10 ng/ml) for 12 h prior to being exposed to either PBS, AlO NSs (125 μg/mL) or AlO NWs (300 μg/mL) for 8 h. Culture supernatants were then collected, centrifuged for 5 min at 5,000 rpm to remove cells and the supernatants was then used to complement the medium used for EMT induction in the cancer cells. HeLa, A549 and SKOV3 cells were seeded at a density of $1*10^4$ cells/cm^2 in 6 well plates after which they were immediately incubated in EMT-induction medium consisting of 50% normal full growth medium and 50% splenocyte-conditioned medium which was supplemented with 1× EMT inducting media supplement (R&D Systems, Minneapolis, MN, USA) after which the cells were left for 3 days. Control experiments occurred similarly, where medium consisted of 50% normal full growth medium and 50% fresh splenocyte growth medium supplemented where the cells were first exposed to the AlO NSs (125 μg/mL) or NWs (300 μg/mL) for 24 h, after which they were exposed to fresh medium supplemented with 1× EMT inducting media supplement.

2.9. Evaluation of EMT induction efficacy

Following EMT induction, HeLa, A549 or SKOV3 cells were fixed in 2% paraformaldehyde, permeabilized using 0.1% Triton X-100 after which they were stained for EMT-specific markers using mouse monoclonal antibodies against E-cadherin, Snail, Vimentin, and Fibronectin (Santa Cruz antibodies, USA; 4 μg/ml, 2 h at room temperature in 10% serum-containing blocking buffer) followed by 3 washes with PBS prior to incubation (1/250 dilution) with secondary antibody (AF633 goat anti-mouse IgG antibody) followed by another 3 washes with PBS and nuclear counterstaining with Hoechst 33342.

2.10. Cell migration and invasion

Following EMT induction, HeLa, A549 or SKOV3 cell types were seeded at a density of $2*10^4$ cells/well, either the Radius™ 24 well cell migration assay plate (Cell BiolabsInc, San Diego, CA, USA) or a collagen IV-coated 8 μm-pore Boyden chamber (Cell BiolabsInc, San Diego, CA, USA). After 24 h, the gel plug was removed from the Radius migration assay plate, allowing the cells to migrate. For cell invasion, the assay procedure was performed in accordance with the manufacturer's instructions.

2.11. Mice experiments

Female DBA/2 mice (Harlan Laboratories, Cambridgeshire, UK), 5–7 weeks old, were used in this study. The animal studies used a syngeneic tumor model in which DBA2 animals received 500,000 KLN 205 cells in 200 μl saline as a subcutaneous injection on the lower part of the left side of the back. All mouse surgical procedures and imaging were performed with the animals anesthetized by inhalation of 2% isoflurane. The condition of the animals was monitored every day and their weight was measured every other day. Tumors were measured with calipers every other day. When tumors reached the size of minimally 50 mm3 (approximately 10–14 days after tumor inoculation), the animals were divided into three different groups for further experiments. One group received an injection of 100 μl saline, the second group received 300 μg AlO NSs while the third group received 300 μg AlO NWs through intravenous injection. After 5 and 10 days, the animals received a second and third bolus of either saline, AlO NWs or NSs, but in both cases this occurred via peritumoral injection. Control animals were animals that either received saline injection instead of the NPs or AlO NW-treated animals receiving dexamethasone at 4 mg/kg bodyweight by intraperitoneal injection 1 h prior to every NP challenge. For the tumor growth studies, all animals were sacrificed 7 weeks after NP administration. All animal studies were approved by KU Leuven's Institutional Animal Care and Use Committee (IACUC; approval number P259/2015) in accordance with the principals and procedures outlined in national and European regulations. Experiments were halted when tumors became larger than 1.5 cm or a deep ulcer was formed, upon which animals were sacrificed. For euthanasia, animals were subjected to 5% isoflurane inhalation. To ensure death following isoflurane inhalation cervical dislocation was performed.

2.12. Clinical chemistry

After 2, 12 or 20 days post initial NP administration, (n = 4 per group per time point), blood samples were withdrawn and serum was collected by centrifuging the whole blood at 3000 rpm for 15 min. Several biochemical parameters, including ALT, AST, CRE, and BUN, were assayed using diagnostic kits purchased through Abcam and experiments were conducted in accordance with the suppliers recommendations.

2.13. Biodistribution studies

At 12 days post initial NP administration, three animals per group were sacrificed and several organs (tumor, liver, spleen, lungs, brains) were resected. The different organs were then exposed to 1.5 mL of aqua regia. The samples were then microwave digested (MLS 1200 Mega, Milestone, Shelton, CT, USA) and appropriately diluted in ultrapure water (>18.2 MΩ cm resistivity). The total amount of Al^{3+} was then measured using ICP-MS as described above for pure NPs.

2.14. Monitoring of tumor growth via optical imaging

Before each imaging session, the mice were injected intraperitoneally with 126 mg/kg D-luciferin (Promega, Madison, WI, USA) dissolved in PBS (15 mg/ml). Next, all 4 animals per group were positioned in the IVIS Spectrum and images were acquired after 10 min under 2% isoflurane inhalation. Images were acquired immediately before the first NP or saline injection and after 5, 10, 15, 21, 28 and 35, 42 and 49 days post first NP injection (medium binning, f stop = 1, time = 25 s). Bioluminescence images were analyzed using the LivingImage (Perkin Elmer, Waltham, MA) processing software. Regions of interest (ROIs) were drawn around the bioluminescent signals in the tumor regions of the mice, and measurements were generated as the total flux (p/s/cm^2/sr) from the selected ROIs.

At 6 and 7 weeks post first NP injection, luminescence imaging was also performed on the chest region of the mice, while the primary tumor was covered by thin layer of black plastic to avoid any light from primary tumor to be detected. Images were acquired similarly as above, but with a longer exposure time (medium binning, f stop = 1, time = 45 s). ROIs were drawn on the chest area of the animal after which the total flux (p/s/cm^2/sr) from the selected ROIs was calculated using the LivingImage processing software.

2.15. Monitoring of NP-mediated inflammation via optical imaging

The level of inflammation was evaluated on the same animals 12 days following first NP administration. All animals received 4 nmol of Cat B 750 FAST (Perkin Elmer, Waltham, MA) through tail vein injection. Cat B 750 FAST is a fluorescent probe that is activated by Cathepsin B activity, mainly present in inflammatory cells or highly metastatic cancers. 3D fluorescence images were acquired 6 h after probe administration, (λ_{ex}: 750 nm, λ_{em}: 770 nm, medium binning, f stop = 1, time = 10 s excitation). Fluorescence images were analyzed using the Living Image (Perkin Elmer, Waltham, MA) processing software, where the threshold level for the fluorescence signal was adjusted to rule out interference of Cat B 750 FAST signal originating from the KLN 205 cells. This threshold was then also applied on the AlO NSs or AlO NWs-treated animals, after which 3D regions of interest (ROIs) were drawn around the tumor regions of the mice (2× diameter of the tumor region in all directions), and measurements were generated as the total flux (p/s/cm^2/sr) from the selected ROIs.

2.16. μCT acquisition

Retrospectively respiratory-gated lung CT data were acquired on a dedicated small animal CT scanner (SkyScan 1076, Bruker CT, Kontich, Belgium). The following scan parameters were used: 50 kVp X-ray source, 0.5 mm aluminium filter, 180 μA current, 120 ms exposure time per projection, 23 × 35 mm^2 field of view (FOV) covering the lung, 9 projections per position with 0.7° increments and a total angle of 180°. The total acquisition time per scan was approximately 13 min, resulting in a reconstructed 3D data set with an isotropic voxel size of (35 × 35 × 35) μm^3.

2.17. Histological examination

At 7 weeks post NP exposure, the animals were sacrificed and the lungs were collected for histological analysis. The lungs were inflated and fixed overnight in 4% paraformaldehyde, followed by paraffin embedding and sectioning into 5 μm-slices, which were then stained with 1% hematoxylin and eosin (H&E).

2.18. Statistical analysis

Statistical analysis was performed using GraphPad Prism 6.0, where all data were analyzed using one-way ANOVA. For statistical significance of any treated group from the control group or between two treated groups under 1 condition, a Dunnett's post-hoc test was applied.

3. Results

3.1. Characterization of AlO nanospheres and nanowires

Low resolution transmission electron microscopy (TEM) images reveal highly crystalline particles both for the AlO NSs and NWs (Fig. 1a and c). In the high resolution TEM image of AlO NSs well resolved crystal lattices in two directions are observed (Fig. 1a3), which is less clear for the NWs, likely due to the small diameter of the latter (Fig. 1c3). The high crystallinity of both NSs and NWs could be confirmed by selected area electron diffraction (SAED) patterns (Fig. 1b and d).

Based on the TEM observations here, the average diameter of the NSs was 36 nm and for the NWs 6 nm diameter and 223 nm length, which is in line with the values provided with the supplier (see Materials and Methods section). The purity of the AlO NPs was then studied using elemental analysis, in which both the NSs and NWs displayed a high purity. No impurities were detected in the NWs (Fig. S1), while the NSs did contain traces of various other elements, including Ti, Cu, In, Si. Quantification of these impurities by inductively coupled plasma-mass spectrometry (ICP-MS) revealed that the AlO NSs had a purity of 94%.

3.2. Pro-inflammatory cytokine release by primary splenocytes at subcytotoxic conditions is predominantly induced by NWs

To investigate the inflammatory effects of the AlO NSs and NWs, primary murine splenocytes were used as an *in vitro* model system (Fig. 2a). These primary cells are a mixture of different cell types, including T cells (26.1%) and macrophages (36.9%) (Fig. S2) and thus present a suitable model to mimic the interactions of the different components of our immune system, rather than a single isolated immune cell type. Toxicity of the AlO NSs and NWs was investigated using previously validated high-content imaging methods, in which cell viability, membrane damage, mitochondrial reactive oxygen species and mitochondrial health were assessed. Fig. 1e–m (Fig. S3) reveals clear-dose dependent toxicity for both

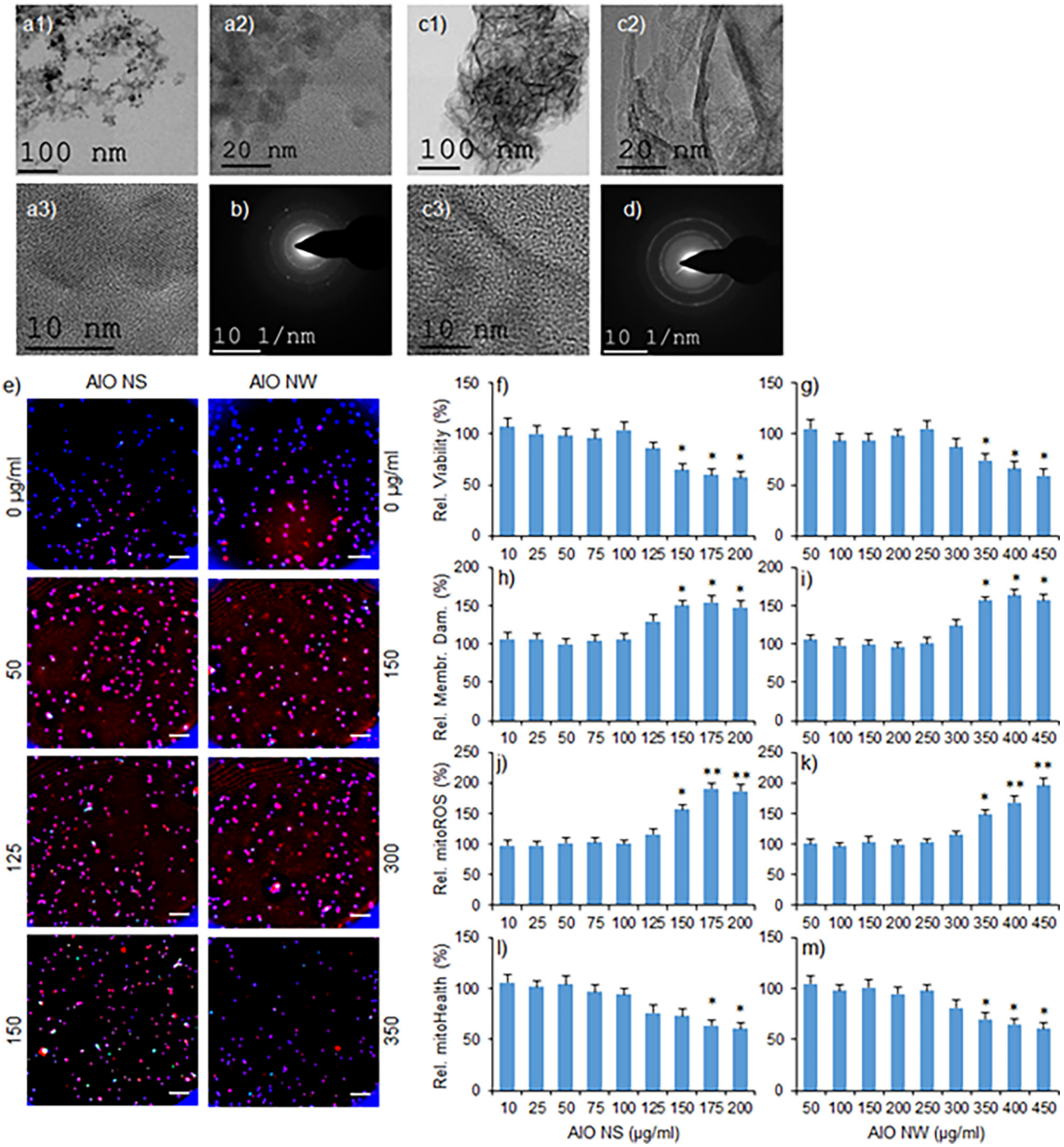

Fig. 1. (a1, a2) Low-resolution TEM images of AlO NS, (c1, c2) AlO NWs, respectively. (a3, c3) High-resolution images of AlO NS and AlO NWs, respectively. The images show highly crystalline particles with well-formed crystal lattices. (b, d) Selected area diffraction patterns of (b) AlO NS and (d) AlO NW. The clear ring patterns in pure and doped particles show highly crystalline particles. (e) Representative high content images of splenocytes either left untreated (0 μg/ml) or exposed to AlO NS (left column) or AlO NW (right column) for 8 h at the concentrations indicated. Cells were stained with an impermeant dead cell stain (green) and Mitotracker CMX Ros (red) and counterstained using Hoechst nuclear counterstaining (blue). Scale bars: 100 μm. (f–m) Histograms revealing the relative level of (f, g) cell viability, (h, i) cell membrane damage, (j, k) mitochondrial ROS, (l, m) mitochondrial health, for splenocytes exposed to AlO NS (f, h, j, l) or AlO NW (g, i, k, m) at the concentrations indicated (8 h exposure) as obtained from the high-content imaging data. Data are shown as relative values after z-normalization compared to untreated control cells (=100%) expressed as mean ± SD ($n = 4$). The degree of significance between samples and control cells is indicated where applicable (*: $p < .05$; **: $p < .01$). (For interpretation of the references to color in this figure legend, the reader is referred to the web version of this article.)

AlO NP types, where significance is reached for the AlO NSs starting at 150 μg/ml and for the NWs at 350 μg/ml. The difference in toxicity between the two NP types may reflect differences in their shape, which will result in different uptake rates [29]. ICP-MS analysis revealed cellular Al^{3+} levels to be 3.8-fold higher for NSs than for NWs, indicating a far higher uptake efficiency of the NSs compared to the NWs. When also taking into account the volume and surface area of the NPs, the toxicity values can be reformulated (Table S1). No clear correlation could be found between the toxicity of the NPs and their total surface area, but toxicity correlated best with the total mass of cell-associated NPs. In line with expectations, both the NWs and NSs were associated far higher with pri-

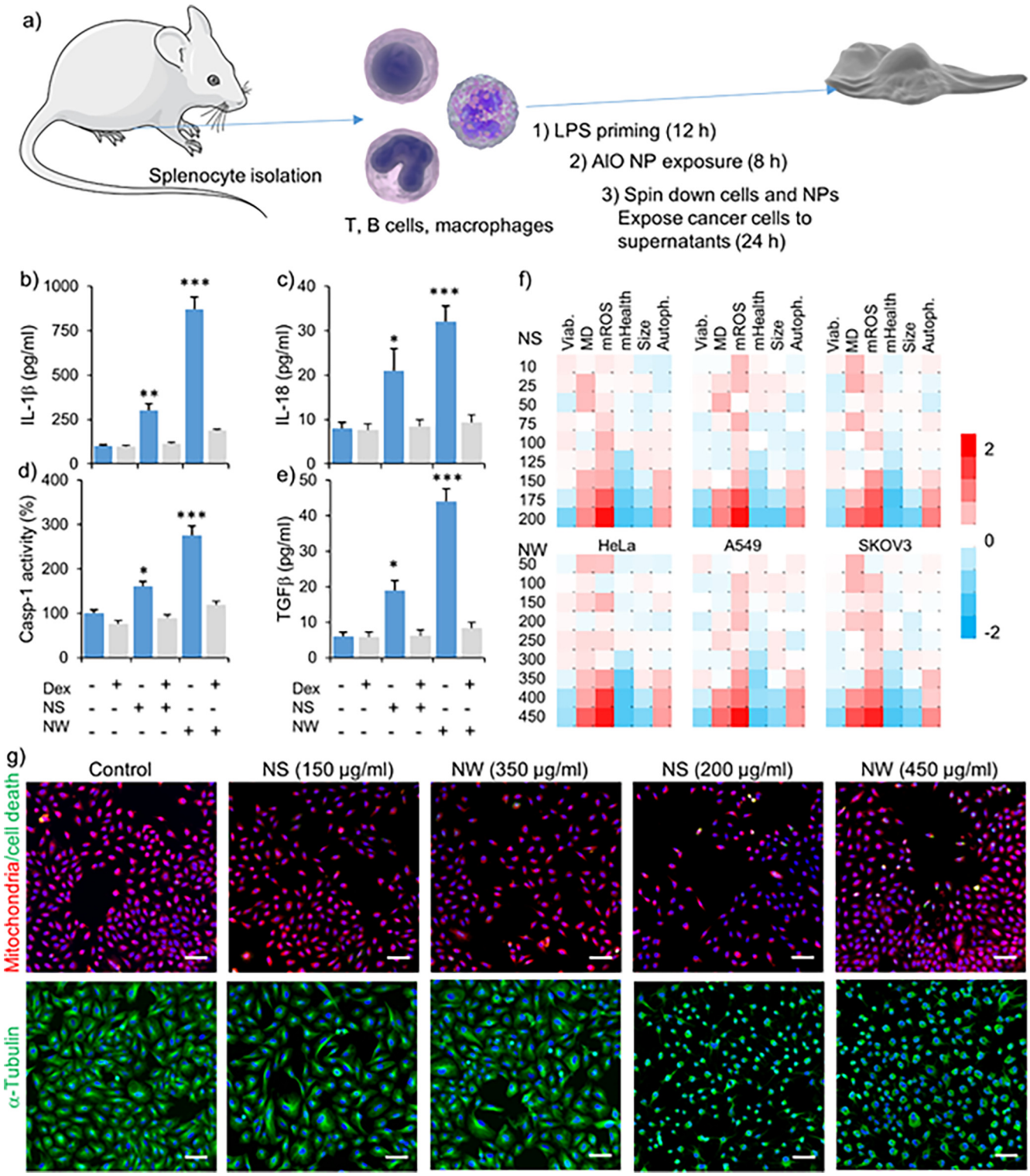

Fig. 2. (a) Schematic overview of the *in vitro* experimental design. (b–e) Histograms representing the level of (b) secreted IL-1β, (c) IL-18, (d) activated Casp-1, (e) secreted TGFβ in splenocytes exposed to subcytotoxic levels of AlO NS (125 μg/ml) or AlO NWs (300 μg/ml) for 8 h in the presence or absence of dexamethasone (100 ng/ml). Data are expressed as mean ± SEM (n = 4). The level of statistical significance is indicated when appropriate (*: $p < .05$; **: $p < .01$; ***: $p < .001$). f) Heat maps of the high content imaging data obtained for HeLa (left), A549 (middle) or SKOV3 cells (right) exposed to various concentrations of AlO NSs (top row) or AlO NWs (bottom row) for 24 h and analyzed for relative cellular health (Viab), membrane damage (MD), mitochondrial ROS (mROS), mitochondrial health (mHealth), cell size (Size) and level of autophagy (Autoph.). Data are shown as relative values after z-normalization compared to untreated control cells (=1) where the fold-change is indicated by the respective color-code. Data have been acquired for a minimum of 5000 cells/condition which were gathered from three independent experiments. (g) Representative high content images of HeLa cells either unexposed or exposed to AlO NSs or NWs at the concentrations indicated. Following exposure, cells were stained with Live Dead cell stain (green: damaged/dead cells), MitoTracker Red CMXRos (red: mitochondrial ROS and health) and nuclei were counterstained with Hoechst (blue) (top row) or stained for α-tubulin (green) and counterstained with Hoechst nuclear stain (blue) (bottom row). Scale bars: 100 μm. (For interpretation of the references to color in this figure legend, the reader is referred to the web version of this article.)

mary macrophages than with T cells (Table S2). This is partly due to the high phagocytic nature of macrophages compared to a more limited endocytic capacity of T cells, along with the fact that the adherent macrophages will be exposed more to sedimenting aggregated nanoparticles than the T cells who remain in suspension.

The immune-modulating effects of the AlO NSs and NWs was then investigated at the highest non-toxic concentrations for both types of NPs (125 μg/ml for NSs and 300 μg/ml for NWs). Both NSs and NWs were found to promote inflammation through activation of the NLRP3 inflammasome, as shown by elevated pro-inflammatory cytokine secretion (IL-1β, IL-18) and activation of Caspase-1 (Casp-1) (Fig. 2b–d). The level of inflammation differed greatly, where NWs were much more potent anti-inflammatory agents than NSs. We also looked into the production of transforming growth factor β (TGFβ), known to possess both pro- as well as anti-inflammatory properties [30]. Similar to the results of the pro-inflammatory cytokines, TGFβ levels were significantly elevated upon exposure to AlO NWs (Fig. 2e). Next, the influence of dexamethasone (DEX) as a potent immunosuppressive molecule that could prevent AlO NPs–induced inflammatory signaling was examined [31]. DEX diminished activity of Casp-1 and secretion of pro-inflammatory cytokines IL-1β and IL-18 as well as TGFβ secretion for both AlO NSs- and AlO NWs-treated cells (Fig. 2b–e).

3.3. NW-exposed primary splenocytes significantly increase in vitro EMT efficacy of various cancer cell lines

The AlO NWs and NSs were then used to label various cancer cell lines, being human cervical carcinoma (HeLa), alveolar epithelial adenocarcinoma (A549) and ovarian epithelial adenocarcinoma (SKOV3) cells. Toxicity thresholds for both the NSs and NWs were higher than those obtained for the primary splenocytes (Fig. 2f and g; Fig. S4), indicating that at the concentrations of 125 μg/ml for NSs and 300 μg/ml for NWs, no significant toxicity occurred on the cancer cells. The NPs did not significantly affect autophagy levels, nor did they affect cell morphology at subcytotoxic concentrations.

TGFβ is an important marker in determining tumor malignancy and is often used as an *in vitro* agent to induce epithelial-to-mesenchymal transition (EMT), a hallmark in the process for tumor metastasis formation [32]. Here, primary splenocytes were exposed to the AlO NSs and NWs at their highest subcytotoxic concentration, after which the cells were centrifuged and the supernatants were added to the culture medium for cancer cells. The cancer cells were then exposed to EMT-inducing growth medium (50%) supplemented with primary splenocyte-conditioned medium (50%) for 3 days, after which the EMT efficacy of the cells was evaluated by staining them for both epithelial (E-cadherin) and mesenchymal (Fibronectin, Snail, Vimentin) markers. Fig. 3a–d reveals a clear increase in EMT efficacy for all three cancer cell types (Fig. 3, Figs. S5–S7) exposed to NW-exposed splenocyte conditioned medium, which was less pronounced when the splenocytes were exposed to the NSs. A similar increase in EMT efficacy could be observed when the cancer cells were exposed to EMT-inducing growth medium supplemented with TGFβ at a similar concentration as the one present in the NWs-exposed splenocyte conditioned medium (Fig. 3e–g). When the splenocytes were treated with DEX during exposure to AlO NSs or NWs, no effect on EMT efficacy could be observed (Fig. 3b–d). No increase in EMT efficacy was observed for cancer cells directly exposed to the NSs or NWs themselves (Fig. 3e–g), suggesting the important role of NP-induced TGFβ-mediated signaling in EMT efficacy. To confirm this, experiments were also repeated in the presence of Galunisertib, a potent and specific inhibitor of TGFβ-receptor signaling, currently undergoing clinical trials in various cancer models, revealing a clear loss of effect of AlO NSs and NWs on EMT efficacy (Fig. S8) [33,34]. Together, these data clearly indicate the role of TGFβ in modulating the EMT efficacy of the cancer cell lines.

The functional role of the EMT process was also investigated by looking into the migration and invasion capacity of the cancer cells. Similarly as for the EMT efficacy, migration capacity and invasiveness of all three cancer cell types significantly increased when the cells were exposed to NW-exposed splenocyte conditioned medium (Fig. 3h–j). No effect of the AlO NPs themselves was observed (Fig. S9), while the increase in migration capacity and invasiveness was lost when the splenocytes were exposed to the AlO NPs in the presence of DEX (Fig. 3h–j). A similar increase could be obtained by supplementing the EMT-inducing growth medium with TGFβ at a similar concentration as the one present in the NWs-exposed splenocyte conditioned medium (Fig. 3h–j). Additionally, we further confirmed the cross-species reactivity of TGFβ be exposing the EMT-induced cancer cells with media that was supplemented with either human or murine TGFβ. This led to no significant differences in the induction efficiency of EMT, indicating that TGFβ in itself is cross-reactive and murine TGFβ as generated by the murine splenocytes can cause elevated EMT in human cancer cells (Fig. S10).

3.4. AlO NWs but not NSs increase tumor inflammation and metastasis in preclinical animal models

To evaluate the *in vivo* effect of the AlO NSs and NWs on tumor metastasis, an immune-competent syngeneic murine model (KLN 205 squamous carcinoma cells in DBA/2 mice) was used. The KLN 205 cells are known to spontaneously metastasize to the lungs and are a highly aggressive tumor cell type [35], thus representing an ideal model to evaluate whether the inflammation induced by the NPs has any effect thereon. Initial *in vitro* studies revealed similar toxicity levels of the AlO NSs and NWs on the KLN 205 cells as for the human cancer cell lines (Fig. 4a). As the chemical EMT induction media is formulated for use on human cells, these experiments could not be repeated on the murine KLN 205 cells. However, it was observed that AlO NWs or NSs also did not affect the migration capacity or invasiveness of the KLN 205 cells (Fig. S9d), while splenocyte-conditioned medium did increase the level of migration and invasiveness, for AlO NW-exposed splenocytes (Fig. 4b). Similar as for the human cancer cells, this increased malignancy could be impeded by DEX (Fig. 4b).

Luminescent KLN 205 cells were then administered subcutaneously in the DBA/2 mice. When the tumor reached 50 mm^3, the animals received either PBS, AlO NWs or NSs (300 μg) via intravenous administration (Fig. 5a). After 5 and 10 days, the animals received a second and third bolus of either PBS, AlO NWs or NSs, but in both cases this occurred via subcutaneous peritumoral injection. Bulk aluminum oxide particles are typically given subcutaneously for adjuvant purposes, in part due to the fact that given their large size, intravenous administration would be risky and not lead to a proper distribution of the aluminum oxide. The advantage of the smaller sized NPs, is the ability to give multiple boluses, in order to properly boost the immune system, enabling both intravenous injection for boosting of the entire peripheral immune system, followed by local administration at the tumor site for enhancing immune activation at the tumor. This mode of administration finally resulted in a high level of the NPs at the tumor site (>50%), and far less in other organs such as liver, spleen and lungs (Fig. S11). The presence of the AlO NSs or NWs did not have any significant effect on liver and kidney function, as assessed by clinical chemistry studies on blood samples at different time points following the first administration of the NPs (Fig. S12). On day 12, inflammation in the animals was measured via *in vivo* optical imaging, revealing a significant increase in tumor-associated

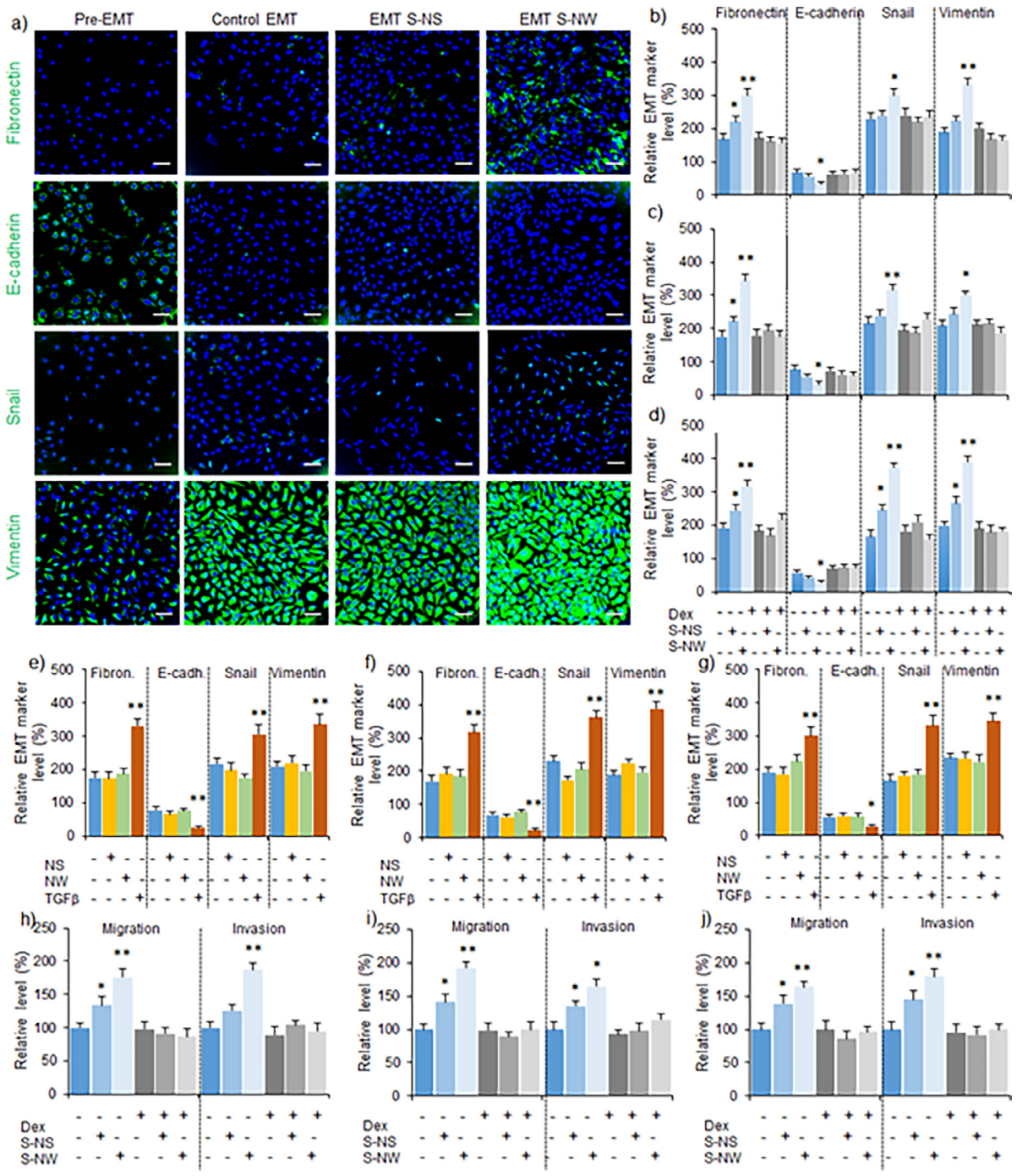

Fig. 3. (a) Representative high content images of HeLa cells either untreated (pre-EMT), or incubated for 3 days with EMT induction medium (control EMT, AlO NS or AlO NWs). The EMT-induced cells were either unexposed or exposed to splenocyte-conditioned medium for primed splenocytes exposed for 8 h to AlO NSs (125 μg/ml) or NWs (300 μg/ml). Cells were stained for EMT markers Fibronectin, E-cadherin, Snail and Vimentin (green). All cells were counterstained with Hoechst nuclear stain (blue). Scale bars: 100 μm. (b–d) Histograms indicating the level of the indicated EMT markers for (b) HeLa, (c) A549 and (d) SKOV3 cells following 3 day EMT induction in the presence or absence of splenocyte-conditioned medium for primed splenocytes exposed, in the presence or absence of dexamethasone (100 ng/ml), for 8 h to AlO NSs (125 μg/ml) or NWs (300 μg/ml). (e–g) Histograms indicating the level of the indicated EMT markers for (e) HeLa, (f) A549 and (g) SKOV3 cells following 3 day EMT induction following direct exposure of the cancer cells to AlO NSs (125 μg/ml) or NWs (300 μg/ml) for 24 h, or treated with TGFβ at 5 pg/ml during 3 days. (b–g) All data are expressed relative to the level of the EMT marker expressed in non-EMT-induced cancer cells. (h–j) Histograms representing relative cell migration and relative cell invasion levels for (h) HeLa, (i) A549, (j) SKOV3 cells following 3 day EMT induction in the presence or absence of splenocyte-conditioned medium for primed splenocytes exposed, in the presence or absence of dexamethasone (100 ng/ml), for 8 h to AlO NSs (125 μg/ml) or NWs (300 μg/ml). The data are expressed relative to those of EMT-induced untreated control cells (100%). (b–j) All data are expressed as mean ± SD ($n = 4$). The degree of statistical significance is indicated when relevant (*: $p < .05$; **: $p < .01$; ***: $p < .001$). Histograms representing the viability of HeLa, KLN 205 or A549 cells exposed to the Ag NPs at 15 μg/ml for prolonged periods of time (1, 2, 3, 4 or 5 days). Data are expressed as mean ± SD ($n = 3$) relative to the viability of untreated control cells (100%). The level of statistical significance is indicated when appropriate (*: $p < .05$). (For interpretation of the references to color in this figure legend, the reader is referred to the web version of this article.)

inflammation in AlO NSs-treated animals, while seven higher levels of inflammation were observed in AlO NWs-treated animals (Fig. 5c and d).

Similar as for the *in vitro* situation, administration of DEX inhibited inflammation to be induced by AlO NWs (Fig. 5c and d). The high level of inflammation around the tumor may impact tumor

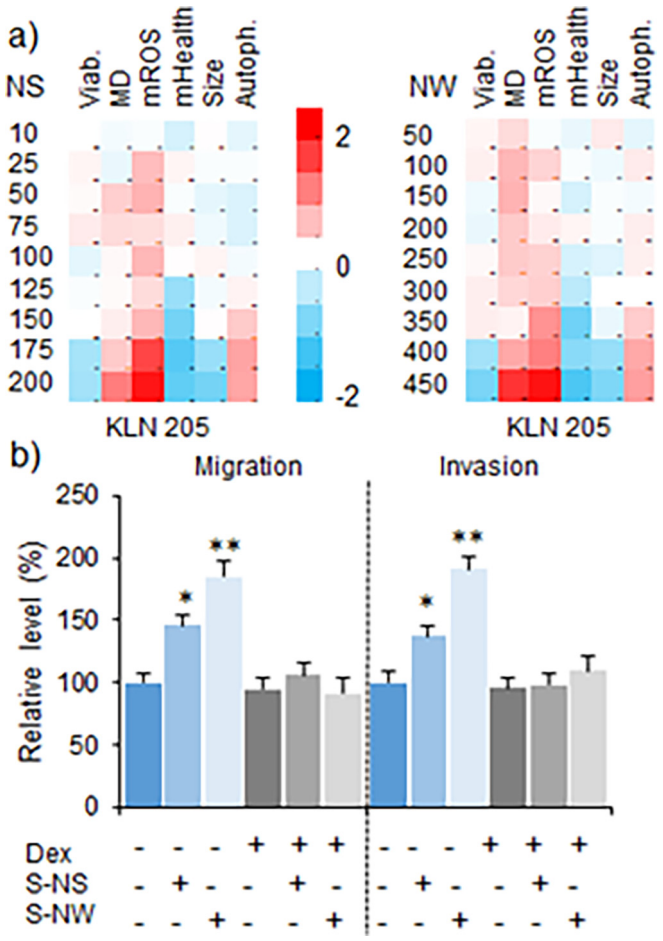

Fig. 4. (a) Heat maps of the high content imaging data obtained for KLN 205 cells exposed to various concentrations of AlO NSs (left column) or AlO NWs (right column) for 24 h and analyzed for relative cellular health (Viab), membrane damage (MD), mitochondrial ROS (mROS), mitochondrial health (mHealth), cell size (Size) and level of autophagy (Autoph.). Data are shown as relative values after z-normalization compared to untreated control cells (=1) where the fold-change is indicated by the respective color-code. Data have been acquired for a minimum of 5000 cells/condition which were gathered from three independent experiments. (b) Histograms representing relative cell migration and relative cell invasion levels for KLN 205 cells following 3 day EMT induction in the presence or absence of splenocyte-conditioned medium for primed splenocytes exposed, in the presence or absence of dexamethasone (100 ng/ml), for 8 h to AlO NSs (125 μg/ml) or NWs (300 μg/ml). The data are expressed as mean ± SD ($n = 4$) relative to those of EMT-induced untreated control cells (100%). The degree of statistical significance is indicated when relevant (*: $p < .05$; **: $p < .01$).

growth and malignancy. Through luminescence imaging, the growth rate of the subcutaneously implanted KLN 205 tumors was found to be slightly but not significantly affected by the AlO NSs or NWs up to at least 7 weeks (Fig. 5e and f).

The occurrence of any spontaneous metastases into the lungs was then also monitored via bioluminescence imaging. After 6 weeks, animals exposed to the NWs displayed some luminescent signals originating from the lung area, which increased after 7 weeks (Fig. 6a and b) and was significantly higher than the level of luminescence originating from the lungs of PBS or NSs-treated animals. To confirm the presence of mature metastases in the lungs, the animals were subjected to small animal computed tomography (μCT), which confirmed the presence of lung lesions in 50% of the NW-treated animals, while no lung lesions were noticed in the saline or NSs-treated animals (Fig. 6c). The reduced inflammation caused by co-treatment of AlO NW exposed animals with DEX reduced the degree of metastatic burden, returning it to control levels (Fig. 6a and b). The influence of TGFβ signaling on the metastasis burden was also confirmed upon co-exposing AlO NW-treated animals with Galunisertib (75 mg/kg body weight) on a daily basis during the period of AlO NW exposure (10 days) which resulted in a clearly reduced degree of metastases (Fig. S13).

After 7 weeks, the primary subcutaneous tumors were growing too large in size, requiring the experiment to be terminated. The *in vivo* results could also be supported by histological analysis of mice lungs, where AlO NSs resulted in the occurrence of a few small metastatic lesions, while AlO NWs resulted in the highest levels of metastatic burden (Fig. 6d). These data were further confirmed as no significant effect could be observed on tumor metastatic burden for animals treated with DEX only or with NS + DEX (Fig. S14). In the present study, the animals were given the same mass of NSs and NWs, but similar results were obtained when animals were given the same amount in terms of number of NPs. When NWs were provided at the same total surface area as the NSs, no effect could be observed anymore, due to the associated lower mass/number of NWs compared to NSs provided (Fig. S15). These data support our findings *in vitro* that the observed effects are linked more to the same mass of NPs than the total surface area.

4. Discussion

In this study, we performed a comprehensive analysis on the impact of differently shaped AlO NPs on immune-modulation and its consequences on tumor malignancy on mammalian cells and in preclinical animal models. We demonstrate that at subcytotoxic concentrations, the AlO NPs, and in particular the high aspect ratio NWs, could significantly increase inflammation and release of pro-inflammatory cytokines, including TGFβ. The latter cytokine affects cancer cell EMT both *in vitro* and *in vivo*, where in preclinical animal models, the occurrence of distal metastases was found to significantly increase upon use of AlO NWs.

The relatively high concentrations of AlO NPs that can be used prior to the onset of any significant toxicity are in line with other reports, which labelled AlO NPs as bio-inert [22]. Comparative studies have found AlO NPs to be less cytotoxic than iron oxide NPs, several of which have also been FDA-approved and have a long history of clinical use [36]. Overall, the higher level of toxicity observed for the NSs is in line with literature data, where spherical AlO NPs had been found to be more cyto- and genotoxic than their high aspect ratio counterparts [22]. This difference has always been linked to differences in their cellular uptake levels, where lower levels of high aspect ratio NWs are typically internalized [37], in line with our results. The lack of a clear correlation between NP surface area and NP toxicity is somewhat surprising, but indicates that toxicity itself is not due to an active surface of AlO NPs. A better correlation could be found for the internalized mass of AlO NPs, where in terms of cell-associated mass, the NWs were slightly more cytotoxic than the NSs. This is likely predominantly ascribed to the shape of the AlO NWs, which can penetrate cellular membranes and hereby cause membrane damage which may result in cell death [10]. From these data, the presence of the metal impurities in the NSs did not seem to contribute extensively to their final toxicity levels, or might even lower it. This is in stark contrast to general findings for carbonaceous materials where impurities, even when present at minute amounts, can drastically affect the toxicity levels of the NPs [38].

The induction of inflammation by AlO is widely known and alum (aluminum hydroxide, phosphate, or hydroxyphosphate) has a long-standing history as an immune adjuvant [39]. Miniaturisation of alum into the nanoscale has been shown to potentiate the proinflammatory capacity [15]. Inflammation in itself has been

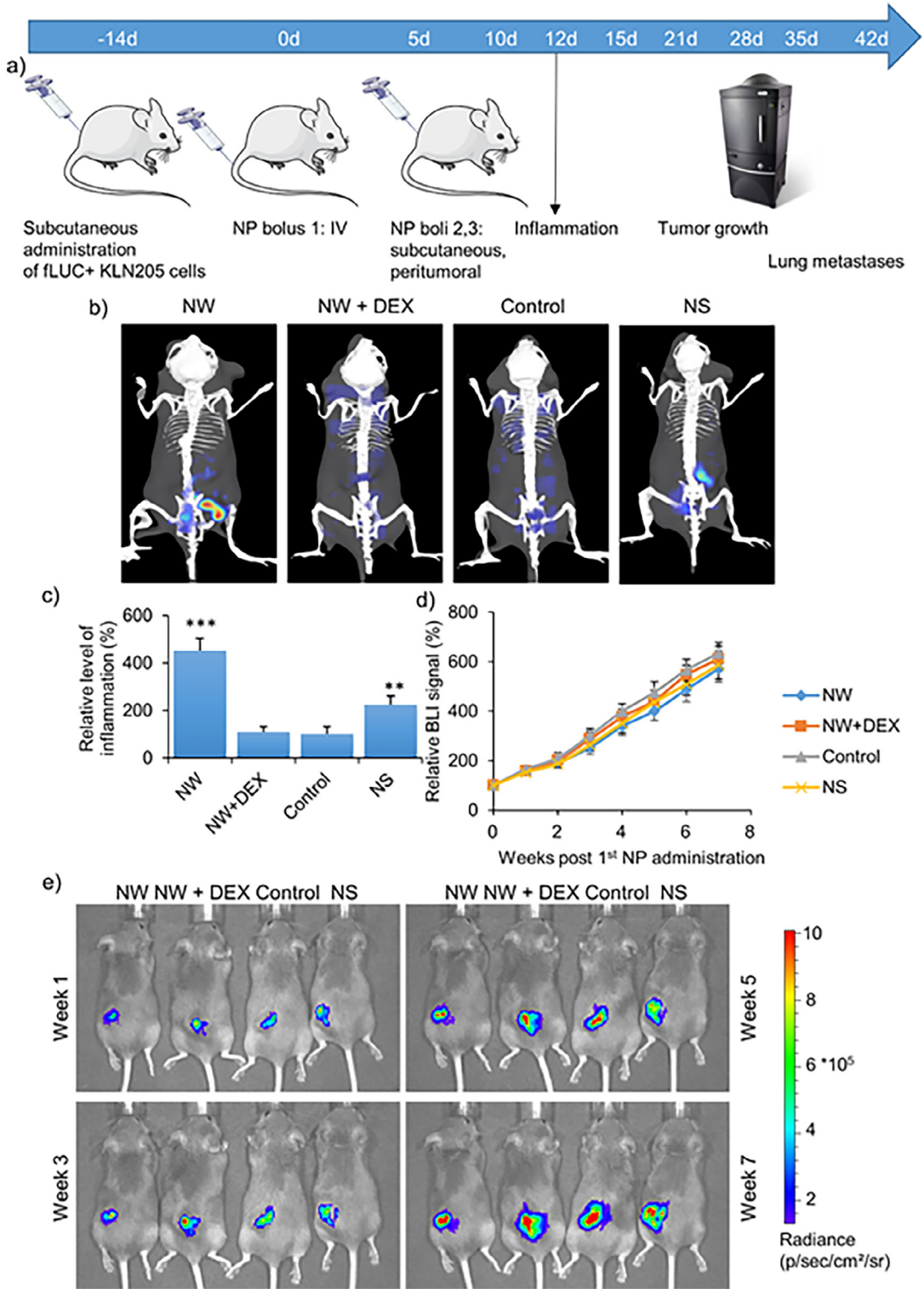

Fig. 5. (a) Schematic overview of the *in vivo* experimental design. (b) Representative *in vivo* optical images of fluorescence signal originating from the inflammation-activatable probe (Cat B 750 FAST) obtained from 3D optical imaging measurements in tumor-bearing DBA/2 mice treated 3 times with AlO NWs, AlO NWs in the presence of dexamethasone, saline (control animals) or AlO NSs. Images were acquired 12 days post initial NP administration. (c) Quantification of the fluorescence signal originating from the inflammation-specific probe. Data are expressed as mean ± SD ($n = 4$) relative to the fluorescence level of saline-treated control animals (=100%). (d) Quantitation of the luciferase signal for DBA/2 mice bearing a subcutaneous fLuc-expressing KLN 205 tumor, and treated 3 times with AlO NWs, AlO NWs in the presence of dexamethasone, saline (control animals) or AlO NSs. The data are expressed as mean ± SD ($n = 4$) relative to the signal of each condition at time point 0 (immediately prior to first NP exposure). (e) Representative optical images of DBA/2 mice subcutaneously transplanted with syngeneic fLuc-expressing KLN 205 cells treated 3 times with AlO NWs, AlO NWs in the presence of dexamethasone, saline (control animals) or AlO NSs. The images are shown after 1, 3, 5 and 7 weeks following initial NP exposure. The signal intensity is indicated by the scale bar provided.

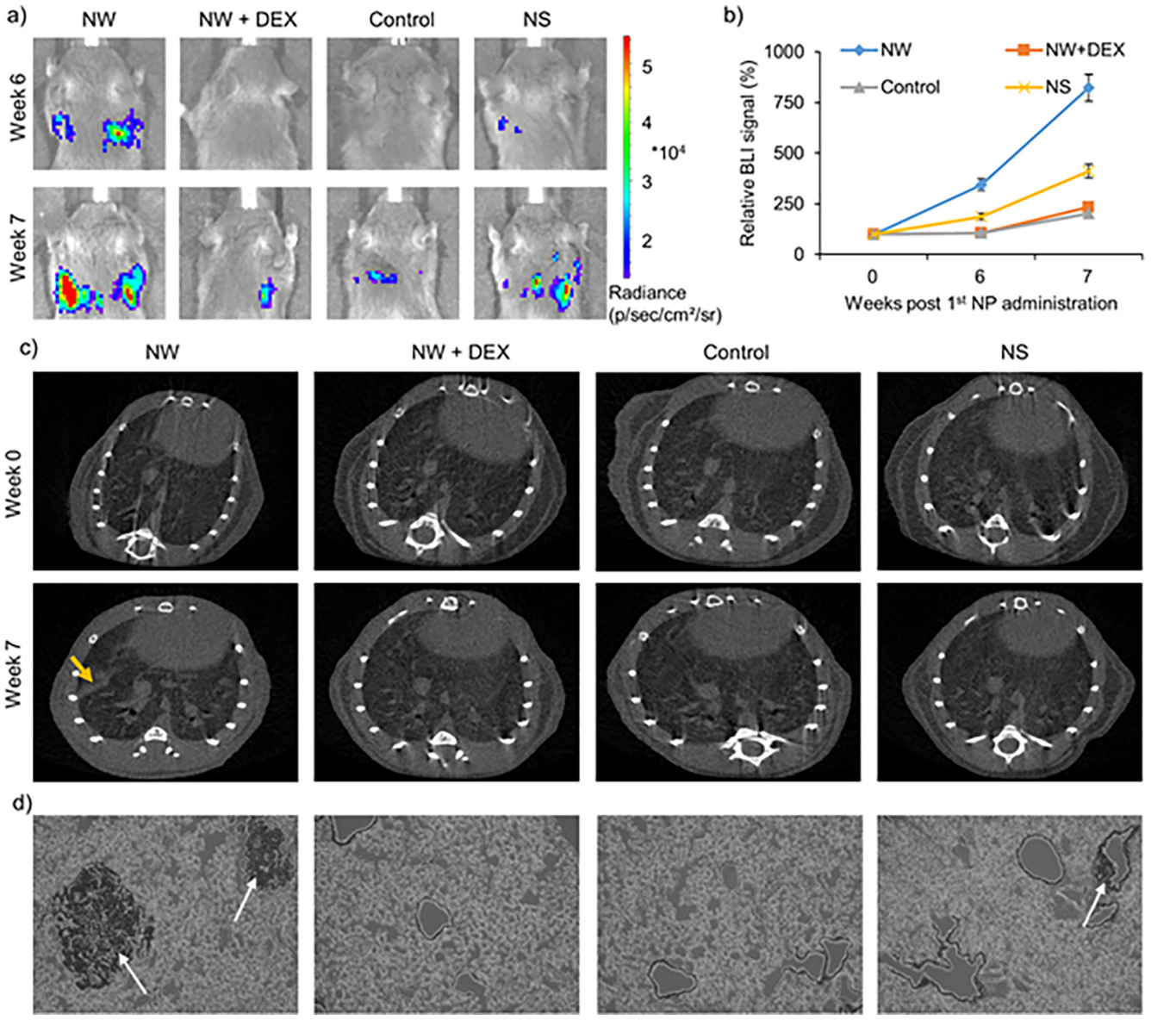

Fig. 6. (a) Representative optical images of DBA/2 mice subcutaneously transplanted with syngeneic fLuc-expressing KLN 205 cells treated 3 times with AlO NWs, AlO NWs in the presence of dexamethasone, saline (control animals) or AlO NSs. The primary tumor region of the animals was shielded by light-impermeant black plastic and signal was acquired from the lung regions of the animals. The images are shown after 6 and 7 weeks following initial NP exposure. The signal intensity is indicated by the scale bar provided. (b) Quantitation of the luciferase signal originating from the lung region of DBA/2 mice bearing a subcutaneous fLuc-expressing KLN 205 tumor, and treated 3 times with AlO NWs, AlO NWs in the presence of dexamethasone, saline (control animals) or AlO NSs after shielding the primary tumors. The data are expressed as mean ± SD (n = 4) relative to the signal of each condition at time point 0 (immediately prior to first NP exposure). (c) Representative μCT images of the lung regions of the treated animals acquired immediately prior to the initial NP administration (top row) and 7 weeks later (bottom row). The presence of metastatic lesions are indicated by yellow arrows. (d) Representative histological sections of the lungs of DBA/2 mice stained with hematoxylin and eosin acquired at a 40× magnification. Metastases are indicated by white arrows. (For interpretation of the references to color in this figure legend, the reader is referred to the web version of this article.)

described to occur mainly by activation of the NLRP3 inflammasome, which has been found to be activated by crystals, such as alumina [40]. This is supported by our findings of caspase-1 activation and elevated IL-1β and IL-18 secretion, which are hallmarks of NLRP3 activation [41]. The higher level of inflammation observed for the high aspect ratio NWs compared to the NSs is also in line with literature, where high aspect ratio NPs are generally more potent in inducing inflammation [5,42]. This has been mainly demonstrated in inhalation studies, where high aspect ratio NPs (*e.g.* nanotubes, nanofibers, nanowires) activate inflammasomes in lung macrophages. The immune altering effect of the AlO NWs can also influence pre-existing inflammation in the host, as some NMs have been shown to alter, for example, allergen-induced eosinophilic inflammation by immunostimulation, immunosuppression, or modulating the balance between Th1, Th2, and Th17 cells, thereby influencing the nature of the inflammatory response [43]. Inflammation in itself is an important hallmark in the onset of cancer, where elevated levels of pro-inflammatory cytokines contribute to tumorigenesis [44].

The elevated secretion of TGFβ was particularly interesting, as the TGFβ signaling pathway is a fundamental pathway playing a primary role in many cellular processes [30]. TGFβ signaling is very complex as it is involved in several counteractive mechanisms, making the final biological outcome hard to predict. In particular for cancer, the influence of TGFβ signaling can be devastating. The TGFβ family of growth regulatory proteins are typical inhibitors of cell growth. As cancers are associated with high levels of cell proliferation, this was expected to be associated with a downregu-

lation of TGFβ signaling. However, in most tumor types, a significant increase in TGFβ expression has been observed and increased expression of TGFβ is accompanied with a change in the signaling pathways to decrease its growth inhibitory effect. High levels of TGFβ are therefore typically associated with higher levels of tumor malignancy [45]. Next to turning from a growth-inhibitory pathway into a growth-stimulating mechanism, TGFβ is also involved in regulating cytoskeletal alterations, through which it can influence EMT efficacy [46]. Cancer malignancy can also be further increased by macrophage-derived TGFβ, which has been shown to impair the function of cytotoxic T cells [47]. Elevated TGFβ levels have been associated with a wide variety of NPs, including nickel oxide [48,49], polystyrene [50] or titanium dioxide [51]. The increase of TGFβ signaling by the NPs has also been associated with pulmonary fibrosis [48,49] or renal inflammation [51]. Here, TGFβ release by the splenocytes stimulated cancer cell EMT on cancer cell lines, while also improving cancer cell migration and invasion. This also led to a marked increase of the metastatic burden in the lungs *in vivo* as demonstrated by optical imaging. Using μCT, lesions could only be observed in the lungs of 50% of the animals treated with AlO NWs, while this was not the case for saline or AlO NSs-treated animals, despite the occurrence of bioluminescence signals in all groups of animals. This may likely be due to the differences in sensitivity between the two methods, where the sensitivity of optical imaging depends on the number of photons emitted from viable cells, while the sensitivity for μCT depends on the spatial resolution of any lesions incurred by the metastatic nodules. Small sized nodules can therefore be too small to be detected by μCT, while they may emit sufficient photons to be detected by optical imaging. This is also confirmed by the histological analysis, where animals treated with AlO NWs showed multiple smaller metastatic nodules, while saline or DEX-treated animals showed nearly no lesions at all. The μCT data enabled us to confirm the presence of metastases in the lungs, which is not possible using optical imaging as no anatomical detail is given. The luminescent signal of the lung metastases does confirm that the lesions observed are in fact metastatic nodules that originate from the primary subcutaneous tumor and are not new tumors that may have developed in the lungs themselves due to the administration of the AlO NPs, as some NPs were found to end up in the lungs (Fig. S7). Other reports on the biodistribution of short and high aspect ratio AlO NPs had demonstrated that upon intravenous administration, the NPs primarily accumulated in the liver and spleen [5]. While increasing the aspect ratio of NP may increase their accumulation in the lung [52], no sign of inflammation around the lung regions was detected. As the second and third bolus of AlO NPs was also administered intratumorally, only minimal amounts are expected to be washed away in the bloodstream and potentially reach the lungs, as most NPs will remain in the tumor region, explaining the highest levels of inflammation there. As the main goal of this study was to investigate the effect of the NMs on tumor growth and the development of metastases, this administration method was selected, first to boost the immune system in general, followed by local administration to evaluate the effect on the tumor itself. This procedure was mainly used to be comparable to future tactics, where targeted nanoformulations would have to be given repeatedly (as common for small molecules) during the therapeutic procedure, triggering potential immune responses at the level of the tumor. However, current nanoformulations generally lack the selectivity and tumor targeting efficacy that would enable repeated intravenous administrations to reach the tumor site in an efficient manner.

As the growth of the tumor did not appear to be significantly affected despite the high levels of inflammation present, this suggests the induction of non-specific inflammation by the NPs, which is in line with their activation of innate immune cells such as macrophages, as has been frequently reported in literature [53,54]. However, a proper anti-tumor immune activation that would provide therapeutic benefit, requires the activation of additional immune cells, such as cytotoxic T cells [55]. In previous work, we have shown that immune activation by silver NPs linked with significant levels of tumor cell death by the same NPs resulted the onset of anti-tumor immunity [56]. The data here suggest that in the absence of any tumor cell death by the NPs, the immune activation is non-specific and does not significantly contribute to any therapeutic outcome. Therefore, the use of NPs and any associated inflammation should be coupled with a potent anti-tumoral affect, as otherwise, the increased inflammation might increase tumor malignancy through enhanced TGFβ signaling.

5. Conclusions

In summary, we demonstrate that high aspect ratio AlO NWs induce higher levels of inflammation than low aspect ratio AlO NSs. The immune-modulating effects of the NPs is shown to have profound effects on cancer cells, where *in vitro* data reveal a clear increase in cancer cell EMT. These data are confirmed in preclinical rodent models, where the degree of tumor-associated inflammation is shown to be elevated, resulting in higher levels of distal metastasis. The data obtained urge for a careful characterization of the biological effect of NPs in the complex multicellular environment and in particular in both normal and disease states, where the NPs can influence any parameter affected by the physiological changes. The results obtained in the present study will be of significant interest to those interested in further developing NPs for anticancer purposes.

Acknowledgments

This work was supported by the FWO-Vlaanderen (S.J.S, KAN 1514716N to B.B.M.), the KU Leuven program financing IMIR (PF 2010/017), the Flemish agency for Innovation through Science and Technology (IWT SBO MIRIAD, IWT SBO NanoComit to U.H.) and by the U.S. Public Health Service Grant, R01 ES016746, with leveraged support from the National Science Foundation and the Environmental Protection Agency under Cooperative AgreementNumber DBI 0830117 and 1266377, EU Commission (MODERN, Contract no. 309314).

Appendix A. Supplementary data

Supplementary data associated with this article can be found, in the online version, at https://doi.org/10.1016/j.actbio.2017.12.020.

References

[1] C. Kinnear, L. Rodriguez-Lorenzo, M.J.D. Clift, B. Goris, S. Bals, B. Rothen-Rutishauser, A. Petri-Fink, Decoupling the shape parameter to assess gold nanorod uptake by mammalian cells, Nanoscale 8 (2016) 16416–16426, https://doi.org/10.1039/C6NR03543D.
[2] B. Tian, X. Zhang, C. Yu, M. Zhou, X. Zhang, The aspect ratio effect of drug nanocrystals on cellular internalization efficiency, uptake mechanisms, and in vitro and in vivo anticancer efficiencies, Nanoscale 7 (2015) 3588–3593, https://doi.org/10.1039/C4NR06743F.
[3] H. Wang, R. Zhao, Y. Li, H. Liu, F. Li, Y. Zhao, G. Nie, Aspect ratios of gold nanoshell capsules mediated melanoma ablation by synergistic photothermal therapy and chemotherapy, nanomedicine nanotechnology, Biol. Med. 12 (2016) 439–448, https://doi.org/10.1016/j.nano.2015.11.013.
[4] E.-J. Park, G.-H. Lee, J.-H. Shim, M.-H. Cho, B.-S. Lee, Y.-B. Kim, J.-H. Kim, Y. Kim, D.-W. Kim, Comparison of the toxicity of aluminum oxide nanorods with different aspect ratio, Arch. Toxicol. 89 (2015) 1771–1782, https://doi.org/10.1007/s00204-014-1332-5.
[5] E.-J. Park, S.N. Kim, M.-S. Kang, B.-S. Lee, C. Yoon, U. Jeong, Y. Kim, G.-H. Lee, D.-W. Kim, J.S. Kim, A higher aspect ratio enhanced bioaccumulation and altered immune responses due to intravenously-injected aluminum oxide

nanoparticles, J. Immunotoxicol. 13 (2016) 439–448, https://doi.org/10.3109/1547691X.2015.1122116.
[6] S. Lin, X. Wang, Z. Ji, C.H. Chang, Y. Dong, H. Meng, Y.-P. Liao, M. Wang, T.-B. Song, S. Kohan, T. Xia, J.I. Zink, S. Lin, A.E. Nel, Aspect ratio plays a role in the hazard potential of CeO2 nanoparticles in mouse lung and zebrafish gastrointestinal tract, ACS Nano 8 (2014) 4450–4464, https://doi.org/10.1021/nn5012754.
[7] J.R. Roberts, R.R. Mercer, R.S. Chapman, G.M. Cohen, S. Bangsaruntip, D. Schwegler-Berry, J.F. Scabilloni, V. Castranova, J.M. Antonini, S.S. Leonard, J.R. Roberts, R.R. Mercer, R.S. Chapman, G.M. Cohen, S. Bangsaruntip, D. Schwegler-Berry, J.F. Scabilloni, V. Castranova, J.M. Antonini, S.S. Leonard, pulmonary toxicity, distribution, and clearance of intratracheally instilled silicon nanowires in rats, J. Nanomater. 2012 (2012) 398302, https://doi.org/10.1155/2012/398302.
[8] C.A. Poland, F. Byrne, W.-S. Cho, A. Prina-Mello, F.A. Murphy, G.L. Davies, J.M.D. Coey, Y. Gounko, R. Duffin, Y. Volkov, K. Donaldson, Length-dependent pathogenic effects of nickel nanowires in the lungs and the peritoneal cavity, Nanotoxicology 6 (2012) 899–911, https://doi.org/10.3109/17435390.2011.626535.
[9] A. Schinwald, K. Donaldson, Use of back-scatter electron signals to visualise cell/nanowires interactions in vitro and in vivo; frustrated phagocytosis of long fibres in macrophages and compartmentalisation in mesothelial cells in vivo, Part. Fibre Toxicol. 9 (2012) 34, https://doi.org/10.1186/1743-8977-9-34.
[10] Y. Wang, G. Kaur, A. Zysk, V. Liapis, S. Hay, A. Santos, D. Losic, A. Evdokiou, Systematic in vitro nanotoxicity study on anodic alumina nanotubes with engineered aspect ratio: understanding nanotoxicity by a nanomaterial model, Biomaterials 46 (2015) 117–130, https://doi.org/10.1016/j.biomaterials.2014.12.008.
[11] C. Bussy, M. Pinault, J. Cambedouzou, M.J. Landry, P. Jegou, M. Mayne-L'hermite, P. Launois, J. Boczkowski, S. Lanone, Critical role of surface chemical modifications induced by length shortening on multi-walled carbon nanotubes-induced toxicity, Part. Fibre Toxicol. 9 (2012) 46, https://doi.org/10.1186/1743-8977-9-46.
[12] B. Sun, X. Wang, Y.-P. Liao, Z. Ji, C.H. Chang, S. Pokhrel, J. Ku, X. Liu, M. Wang, D. R. Dunphy, R. Li, H. Meng, L. Mädler, C.J. Brinker, A.E. Nel, T. Xia, Repetitive dosing of fumed silica leads to profibrogenic effects through unique structure-activity relationships and biopersistence in the lung, ACS Nano 10 (2016) 8054–8066, https://doi.org/10.1021/acsnano.6b04143.
[13] B. Sun, S. Pokhrel, D.R. Dunphy, H. Zhang, Z. Ji, X. Wang, M. Wang, Y.-P. Liao, C. H. Chang, J. Dong, R. Li, L. Mädler, C.J. Brinker, A.E. Nel, T. Xia, Reduction of acute inflammatory effects of fumed silica nanoparticles in the lung by adjusting silanol display through calcination and metal doping, ACS Nano 9 (2015) 9357–9372, https://doi.org/10.1021/acsnano.5b03443.
[14] D. Losic, S. Simovic, Self-ordered nanopore and nanotube platforms for drug delivery applications, Expert Opin. Drug Delivery 6 (2009) 1363–1381, https://doi.org/10.1517/17425240903300857.
[15] Z. Sun, W. Wang, R. Wang, J. Duan, Y. Hu, J. Ma, J. Zhou, S. Xie, X. Lu, Z. Zhu, S. Chen, Y. Zhao, H. Xu, C. Wang, X.-D. Yang, Aluminum nanoparticles enhance anticancer immune response induced by tumor cell vaccine, Cancer Nanotechnol. 1 (2010) 63–69, https://doi.org/10.1007/s12645-010-0001-5.
[16] A. Frey, N. Mantis, P.A. Kozlowski, A.J. Quayle, A. Bajardi, J.J. Perdomo, F.A. Robey, M.R. Neutra, Immunization of mice with peptomers covalently coupled to aluminum oxide nanoparticles, Vaccine 17 (1999) 3007–3019 (accessed 5.10.16).
[17] J. Giri, A. Ray, S. Dasgupta, D. Datta, D. Bahadur, Investigation on Tc tuned nano particles of magnetic oxides for hyperthermia applications, Biomed. Mater. Eng. 13 (2003) 387–399 (accessed 5.10.16).
[18] L.G. Gutwein, T.J. Webster, Osteoblast and chrondrocyte proliferation in the presence of alumina and titania nanoparticles, J. Nanopart. Res. 4 (2002) 231–238, https://doi.org/10.1023/A:1019920105207.
[19] A. Yamamoto, R. Honma, M. Sumita, T. Hanawa, Cytotoxicity evaluation of ceramic particles of different sizes and shapes, J. Biomed. Mater. Res. A 68 (2004) 244–256, https://doi.org/10.1002/jbm.a.20020.
[20] L.G. Parkinson, N.L. Giles, K.F. Adcroft, M.W. Fear, F.M. Wood, G.E. Poinern, The potential of nanoporous anodic aluminium oxide membranes to influence skin wound repair, Tissue Eng. Part A 15 (2009) 3753–3763, https://doi.org/10.1089/ten.TEA.2008.0594.
[21] F. Buyukserin, C.R. Martin, The use of reactive ion etching for obtaining "free" silica nano test tubes, Appl. Surf. Sci. 256 (2010) 7700–7705, https://doi.org/10.1016/j.apsusc.2010.06.040.
[22] M. Hashimoto, J.-I. Sasaki, S. Imazato, Investigation of the cytotoxicity of aluminum oxide nanoparticles and nanowires and their localization in L929 fibroblasts and RAW264 macrophages, J. Biomed. Mater. Res. B Appl. Biomater. 104 (2016) 241–252, https://doi.org/10.1002/jbm.b.33377.
[23] M. Bruchard, C. Rebé, V. Derangère, D. Togbé, B. Ryffel, R. Boidot, E. Humblin, A. Hamman, F. Chalmin, H. Berger, A. Chevriaux, E. Limagne, L. Apetoh, F. Végran, F. Ghiringhelli, The receptor NLRP3 is a transcriptional regulator of TH2 differentiation, Nat. Immunol. 16 (2015) 859–870, https://doi.org/10.1038/ni.3202.
[24] A. Baroja-Mazo, F. Martín-Sánchez, A.I. Gomez, C.M. Martínez, J. Amores-Iniesta, V. Compan, M. Barberà-Cremades, J. Yagüe, E. Ruiz-Ortiz, J. Antón, S. Buján, I. Couillin, D. Brough, J.I. Arostegui, P. Pelegrín, The NLRP3 inflammasome is released as a particulate danger signal that amplifies the inflammatory response, Nat. Immunol. 15 (2014) 738–748, https://doi.org/10.1038/ni.2919.
[25] N. Kumari, B.S. Dwarakanath, A. Das, A.N. Bhatt, Role of interleukin-6 in cancer progression and therapeutic resistance, Tumor Biol. 37 (2016) 11553–11572, https://doi.org/10.1007/s13277-016-5098-7.
[26] B.B. Manshian, S. Munck, P. Agostinis, U. Himmelreich, S.J. Soenen, High content analysis at single cell level identifies different cellular responses dependent on nanomaterial concentrations, Sci. Rep. 5 (2015) 13890, https://doi.org/10.1038/srep13890.
[27] B.B. Manshian, D.F. Moyano, N. Corthout, S. Munck, U. Himmelreich, V.M. Rotello, S.J. Soenen, High-content imaging and gene expression analysis to study cell-nanomaterial interactions: the effect of surface hydrophobicity, Biomaterials 35 (2014) 9941–9950.
[28] B.B. Manshian, C. Pfeiffer, B. Pelaz, T. Heimerl, M. Gallego, M. Möller, P. Del Pino, U. Himmelreich, W.J. Parak, S.J. Soenen, High-content imaging and gene expression approaches to unravel the effect of surface functionality on cellular interactions of silver nanoparticles, ACS Nano 9 (2015) 10431–10444, https://doi.org/10.1021/acsnano.5b04661.
[29] X. Huang, X. Teng, D. Chen, F. Tang, J. He, The effect of the shape of mesoporous silica nanoparticles on cellular uptake and cell function, Biomaterials 31 (2010) 438–448, https://doi.org/10.1016/j.biomaterials.2009.09.060.
[30] K. Abnaof, N. Mallela, G. Walenda, S.K. Meurer, K. Seré, Q. Lin, B. Smeets, K. Hoffmann, W. Wagner, M. Zenke, R. Weiskirchen, H. Fröhlich, TGF-β stimulation in human and murine cells reveals commonly affected biological processes and pathways at transcription level, BMC Syst. Biol. 8 (2014) 55, https://doi.org/10.1186/1752-0509-8-55.
[31] A. Naji, B.A. Muzembo, K.-I. Yagyu, N. Baba, F. Deschaseaux, L. Sensebé, N. Suganuma, Endocytosis of indium-tin-oxide nanoparticles by macrophages provokes pyroptosis requiring NLRP3-ASC-Caspase1 axis that can be prevented by mesenchymal stem cells, Sci. Rep. 6 (2016) 26162, https://doi.org/10.1038/srep26162.
[32] Y. Wang, B.P. Zhou, Epithelial-mesenchymal transition--a hallmark of breast cancer metastasis, Cancer Hallm. 1 (2013) 38–49, https://doi.org/10.1166/ch.2013.1004.
[33] H.C. Tran, Z. Wan, M.A. Sheard, J. Sun, J.R. Jackson, J. Malvar, Y. Xu, L. Wang, R. Sposto, E.S. Kim, S. Asgharzadeh, R.C. Seeger, TGFβR1 blockade with galunisertib (LY2157299) enhances anti-neuroblastoma activity of the anti-GD2 antibody dinutuximab (ch14.18) with natural killer cells, Clin. Cancer Res. 23 (2017) 804–813, https://doi.org/10.1158/1078-0432.CCR-16-1743.
[34] A.A. Brandes, A.F. Carpentier, S. Kesari, J.M. Sepulveda-Sanchez, H.R. Wheeler, O. Chinot, L. Cher, J.P. Steinbach, D. Capper, P. Specenier, J. Rodon, A. Cleverly, C. Smith, I. Gueorguieva, C. Miles, S.C. Guba, D. Desaiah, M.M. Lahn, W. Wick, A Phase II randomized study of galunisertib monotherapy or galunisertib plus lomustine compared with lomustine monotherapy in patients with recurrent glioblastoma, Neuro. Oncol. 18 (2016) 1146–1156, https://doi.org/10.1093/neuonc/now009.
[35] D.J. Boffa, F. Luan, D. Thomas, H. Yang, V.K. Sharma, M. Lagman, M. Suthanthiran, Rapamycin inhibits the growth and metastatic progression of non-small cell lung cancer, Clin. Cancer Res. 10 (2004) 293–300 (accessed 5.10.16).
[36] S. Rajiv, J. Jerobin, V. Saranya, M. Nainawat, A. Sharma, P. Makwana, C. Gayathri, L. Bharath, M. Singh, M. Kumar, A. Mukherjee, N. Chandrasekaran, Comparative cytotoxicity and genotoxicity of cobalt (II, III) oxide, iron (III) oxide, silicon dioxide, and aluminum oxide nanoparticles on human lymphocytes in vitro, Hum. Exp. Toxicol. 35 (2016) 170–183, https://doi.org/10.1177/0960327115579208.
[37] Y. Qiu, Y. Liu, L. Wang, L. Xu, R. Bai, Y. Ji, X. Wu, Y. Zhao, Y. Li, C. Chen, Surface chemistry and aspect ratio mediated cellular uptake of Au nanorods, Biomaterials 31 (2010) 7606–7619, https://doi.org/10.1016/j.biomaterials.2010.06.051.
[38] P. Kumarathasan, D. Breznan, D. Das, M.A. Salam, Y. Siddiqui, C. MacKinnon-Roy, J. Guan, N. de Silva, B. Simard, R. Vincent, Cytotoxicity of carbon nanotube variants: a comparative *in vitro* exposure study with A549 epithelial and J774 macrophage cells, Nanotoxicology 9 (2015) 148–161, https://doi.org/10.3109/17435390.2014.902519.
[39] P. He, Y. Zou, Z. Hu, Advances in aluminum hydroxide-based adjuvant research and its mechanism, Hum. Vaccine Immunother. 11 (2015) 477–488, https://doi.org/10.1080/21645515.2014.1004026.
[40] V. Hornung, F. Bauernfeind, A. Halle, E.O. Samstad, H. Kono, K.L. Rock, K.A. Fitzgerald, E. Latz, Silica crystals and aluminum salts activate the NALP3 inflammasome through phagosomal destabilization, Nat. Immunol. 9 (2008) 847–856, https://doi.org/10.1038/ni.1631.
[41] S.J. Lalor, L.S. Dungan, C.E. Sutton, S.A. Basdeo, J.M. Fletcher, K.H.G. Mills, Caspase-1-processed cytokines IL-1beta and IL-18 promote IL-17 production by gammadelta and CD4 T cells that mediate autoimmunity, J. Immunol. 186 (2011) 5738–5748, https://doi.org/10.4049/jimmunol.1003597.
[42] B. Sun, X. Wang, Z. Ji, M. Wang, Y.-P. Liao, C.H. Chang, R. Li, H. Zhang, A.E. Nel, T. Xia, NADPH oxidase-dependent NLRP3 inflammasome activation and its important role in lung fibrosis by multiwalled carbon nanotubes, Small 11 (2015) 2087–2097, https://doi.org/10.1002/smll.201402859.
[43] E.A. Thompson, B.C. Sayers, E.E. Glista-Baker, K.A. Shipkowski, A.J. Taylor, J.C. Bonner, Innate immune responses to nanoparticle exposure in the lung, J. Environ. Immunol. Toxicol. 1 (2014) 150–156, https://doi.org/10.7178/jeit.23.
[44] A. Mantovani, Molecular pathways linking inflammation and cancer, Curr. Mol. Med. 10 (2010) 369–373 (accessed 24.8.16).
[45] L.I. Gold, The role for transforming growth factor-beta (TGF-beta) in human cancer, Crit. Rev. Oncog. 10 (1999) 303–360 (accessed 5.10.16).

[46] K.E. Bachman, B.H. Park, Duel nature of TGF-beta signaling: tumor suppressor vs. tumor promoter, Curr. Opin. Oncol. 17 (2005) 49–54 (accessed 5.10.16).
[47] L. Li, L. Yang, L. Wang, F. Wang, Z. Zhang, J. Li, D. Yue, X. Chen, Y. Ping, L. Huang, B. Zhang, Y. Zhang, Impaired T cell function in malignant pleural effusion is caused by TGF-β derived predominantly from macrophages, Int. J. Cancer 139 (2016) 2261–2269, https://doi.org/10.1002/ijc.30289.
[48] F. Qian, M. He, W. Duan, L. Mao, Q. Li, Z. Yu, Z. Zhou, Y. Zhang, Cross regulation between hypoxia-inducible transcription factor-1α (HIF-1α) and transforming growth factor (TGF)-ß1 mediates nickel oxide nanoparticles (NiONPs)-induced pulmonary fibrosis, Am. J. Transl. Res. 7 (2015) 2364–2378 (accessed 5.10.16).
[49] X.H. Chang, A. Zhu, F.F. Liu, L.Y. Zou, L. Su, S.K. Liu, H.H. Zhou, Y.Y. Sun, A.J. Han, Y.F. Sun, S. Li, J. Li, Y.B. Sun, Nickel oxide nanoparticles induced pulmonary fibrosis via TGF-β1 activation in rats, Hum. Exp. Toxicol. (2016), https://doi.org/10.1177/0960327116666650.
[50] A.-K. Fuchs, T. Syrovets, K.A. Haas, C. Loos, A. Musyanovych, V. Mailänder, K. Landfester, T. Simmet, Carboxyl- and amino-functionalized polystyrene nanoparticles differentially affect the polarization profile of M1 and M2 macrophage subsets, Biomaterials 85 (2016) 78–87, https://doi.org/10.1016/j.biomaterials.2016.01.064.
[51] F. Hong, N. Wu, Y. Ge, Y. Zhou, T. Shen, Q. Qiang, Q. Zhang, M. Chen, Y. Wang, L. Wang, J. Hong, Nanosized titanium dioxide resulted in the activation of TGF-β/Smads/p38MAPK pathway in renal inflammation and fibration of mice, J. Biomed. Mater. Res. A 104 (2016) 1452–1461, https://doi.org/10.1002/jbm.a.35678.
[52] T. Yu, D. Hubbard, A. Ray, H. Ghandehari, In vivo biodistribution and pharmacokinetics of silica nanoparticles as a function of geometry, porosity and surface characteristics, J. Control Release 163 (2012) 46–54, https://doi.org/10.1016/j.jconrel.2012.05.046.
[53] V. Mishra, V. Baranwal, R.K. Mishra, S. Sharma, B. Paul, A.C. Pandey, Titanium dioxide nanoparticles augment allergic airway inflammation and Socs3 expression via NF-κB pathway in murine model of asthma, Biomaterials 92 (2016) 90–102, https://doi.org/10.1016/j.biomaterials.2016.03.016.
[54] Y. Lu, S. Xu, H. Chen, M. He, Y. Deng, Z. Cao, H. Pi, C. Chen, M. Li, Q. Ma, P. Gao, Y. Ji, L. Zhang, Z. Yu, Z. Zhou, CdSe/ZnS quantum dots induce hepatocyte pyroptosis and liver inflammation via NLRP3 inflammasome activation, Biomaterials 90 (2016) 27–39, https://doi.org/10.1016/j.biomaterials.2016.03.003.
[55] M.H. Spitzer, Y. Carmi, N.E. Reticker-Flynn, S.S. Kwek, D. Madhireddy, M.M. Martins, P.F. Gherardini, T.R. Prestwood, J. Chabon, S.C. Bendall, L. Fong, G.P. Nolan, E.G. Engleman, Systemic immunity is required for effective cancer immunotherapy, Cell 168 (2017) 487–502 e15, https://doi.org/10.1016/j.cell.2016.12.022.
[56] B.B. Manshian, J. Jimenez, U. Himmelreich, S.J. Soenen, Presence of an immune system increases anti-tumor effect of Ag nanoparticle treated mice, Adv. Healthcare Mater. 6 (2017) 1601099, https://doi.org/10.1002/adhm.201601099.